



# **JGR** Solid Earth

## RESEARCH ARTICLE

10.1029/2023JB028509

## **Key Points:**

- We developed a laboratory technique to generate heterogeneous friction properties and contained fault ruptures without using gouge
- Three different slip modes were found as a function of L/h\*: (a) aseismic slip,
   (b) periodic slip, and (c) non-periodic slip
- Ruptures stopped or slowed by velocity-strengthening fault sections are closer to natural earthquakes than standard, complete-rupture events

#### **Supporting Information:**

Supporting Information may be found in the online version of this article.

#### Correspondence to:

G. C. McLaskey, gcm8@cornell.edu

#### Citation:

Song, J. Y., & McLaskey, G. C. (2024). Laboratory earthquake ruptures contained by velocity strengthening fault patches. *Journal of Geophysical Research: Solid Earth*, 129, e2023JB028509. https://doi. org/10.1029/2023JB028509

Received 8 DEC 2023 Accepted 30 MAR 2024

## **Author Contributions:**

Conceptualization: Gregory
C. McLaskey
Formal analysis: Jun Young Song
Funding acquisition: Gregory
C. McLaskey
Investigation: Jun Young Song

Methodology: Jun Young Song Resources: Gregory C. McLaskey Supervision: Gregory C. McLaskey Writing – original draft: Jun Young Song Writing – review & editing: Gregory C. McLaskey

© 2024. American Geophysical Union. All Rights Reserved.

# **Laboratory Earthquake Ruptures Contained by Velocity Strengthening Fault Patches**

Jun Young Song<sup>1</sup> and Gregory C. McLaskey<sup>1</sup>

<sup>1</sup>School of Civil and Environmental Engineering, Cornell University, Ithaca, NY, USA

**Abstract** Many natural faults are believed to consist of velocity weakening (VW) patches surrounded by velocity strengthening (VS) sections. Numerical studies routinely employ this framework to study earthquake sequences including repeating earthquakes. In this laboratory study, we made a VW asperity, of length L, from a bare Poly(methyl methacrylate) PMMA frictional interface and coated the surrounding interface with Teflon to make VS fault sections. Behavior of this isolated asperity was studied as a function of L (ranging from 100 to 400 mm) and the critical nucleation length,  $h^*$ , which is inversely proportional to the applied normal stress (2-16 MPa). Consistent with recent numerical simulations, we observed assismic slip for  $L/h^* < 2$ , periodic slip for  $2 < L/h^* < 6$ , and non-periodic slip for  $10 < L/h^*$ . Furthermore, we compared the experiments where L was contained by VS material to standard stick-slip events where L was bounded by free surfaces (i.e., L = the total sample length). The free surface case produced  $\sim 10$  times larger slip during stickslip events compared to the contained fault ruptures, even with identical  $L/h^*$ . This disparity highlights how standard, complete-rupture stick-slip events differ from contained events expected in nature, due to both the free surface conditions and the heterogeneous normal stress along the fault near the free ends, as confirmed by Digital Image Correlation analysis. This study not only introduces the Teflon coating experimental technique for containing laboratory earthquake ruptures, but also highlights the utility of  $L/h^*$  as a predictive parameter for earthquake behavior.

**Plain Language Summary** Earthquakes are often modeled as a central fault section that slips seismically surrounded by a region that creeps slowly and generally stops earthquake ruptures. The central fault section weakens with increasing slip velocity, and is thus velocity weakening (VW). Surrounding regions strengthen and are velocity strengthening (VS). In this laboratory study, we used the glassy polymer PMMA for the VW section and coated the PMMA with Teflon to create the VS sections. We changed the size (L) of the VW area and the applied normal stress to the fault, which is proportional to  $L/h^*$ , where  $h^*$  is an earthquake nucleation length scale. With either an increase of applied normal stress or an increase in the size of the VW region (larger  $L/h^*$ ), the slip behavior changed from stable slip to periodic slow events to faster and more irregular stick-slip events. Fault ruptures not contained by the VS material, where the VW section extended all the way to the sample ends, made larger slip events that did not radiate seismic waves as efficiently with fault slip as expected for natural earthquakes. This shows that contained events are more similar to natural earthquakes than standard uncontained stick-slip events.

## 1. Introduction

Fault zones are composed of various minerals which can be divided into two main classes: velocity strengthening (VS) fault sections that slide stably and velocity weakening (VW) fault sections that slip unstably and nucleate earthquakes (Dieterich, 1992; Rice & Ruina, 1983). Depending on the arrangement of VS and VW sections, a variety of earthquake behavior has been observed on the same fault. In subduction zones, for example, there is a locked zone (VW) that causes megathrust earthquakes and also other zones, usually in shallower or deeper areas (VS) that produce slow slip events (Ito et al., 2007; Obara & Kato, 2016; Obara et al., 2004; Wallace et al., 2016). Slow slip is also found on transform boundaries in the San Andreas fault system within the serpentine zones, creeping at ~30 mm/yr (Moore & Rymer, 2007; Titus et al., 2006). Therefore, VS and VW materials are prevalently distributed in natural faults.

Advances in numerical simulation have provided valuable insights into the diverse slip behavior that can occur on heterogeneous faults (e.g., Luo & Ampuero, 2018). In particular, if the length (L) of a single VW fault section (i.e., seismic asperity) surrounded by VS sections is less than the critical nucleation length scale  $(h^*)$ , then only

SONG AND MCLASKEY 1 of 16

quasi-stable sliding occurs. Both slow and fast ruptures occur when  $L \approx h^*$  (Veedu & Barbot, 2016). As the ratio  $L/h^*$  increases, a wide range of slip behaviors is observed, ranging from periodic slow slips to chaotic fast ruptures (Barbot, 2019). Simulations involving multiple asperities have been employed to study complex natural faults (Luo & Ampuero, 2018; Nakata et al., 2011).

Laboratory experiments also explored this behavior. Fault gouges of different composition were employed to make a VW fault section surrounded by VS gouges (Bedford et al., 2022; Buijze et al., 2021). However, these experiments showed that nonuniform compaction of the gouges can cause heterogeneous normal stress distributions that complicate the interpretation of the results (Buijze et al., 2020, 2021). Despite this added complexity, those authors do see rupture confinement in the VS patches, as well as transitional slip modes from aseismic to seismic as a function of  $L/h^*$  that are generally consistent with theory and numerical models.

More commonly, lab experiments use a VW fault surface using rocks or plastic materials, surrounded by the free surfaces of the sample (i.e., L = total sample length). These experiments also reported fast and slow stick-slip events (Leeman et al., 2016; Mclaskey & Yamashita, 2017; Mei et al., 2021, 2022; Yamashita et al., 2022). However, in this case, the free ends of the sample are more unstable than the interior of the sample, so the fault ends can act as asperities (Cebry et al., 2022), which does not correctly simulate natural seismic zones.

In this study, we contained the dynamic rupture using a Teflon VS surface treatment on a 760 mm long PMMA sample and used a bare PMMA/PMMA section as a VW asperity. We investigated the slip behavior in relation to  $L/h^*$  by adjusting both the size L of the VW patch and the applied normal stress  $(\sigma_n)$  (since  $h^* \sim 1/\sigma_n$ , see Section 2). We observed assismic slip at  $L/h^* < 2$ , periodic slip at  $2 < L/h^* < 6$ , and non-periodic at  $L/h^* > 10$ . Furthermore, we compared the contained and partially contained slip behavior to that of a free fault (FF) without VS material on the ends.

## 2. Theory of Nucleation Length

The behavior of fault systems is frequently modeled using rate-and-state friction (RSF), an empirical relationship, expressed as (Dieterich, 1979):

$$\mu = \mu' + a \ln \frac{V}{V'} + b \ln \frac{V'\theta}{D_c} \tag{1}$$

where  $\mu$  is the friction coefficient, a and b are constitutive RSF parameters, V is the slip velocity,  $\mu'$  is the reference friction coefficient, V' is the reference slip velocity,  $\theta$  is a state variable related to the contact age, and  $D_c$  is the characteristic slip weakening distance. The aging law, which captures the process of contact healing (Marone, 1998), is:

$$\frac{d\theta}{dt} = 1 - \frac{V\theta}{D_c},\tag{2}$$

though other forms of Equation 2, such as the slip law, are also common. For the steady-state sliding  $(d\theta/dt = 0)$  and  $V\theta/D_c = 1$ , Equation 1 reduces to

$$\mu = \mu' + (a - b) \ln \frac{V}{V'}.$$
 (3)

When considering fault stability, the factor (a - b) plays a crucial role (Dieterich & Kilgore, 1994; Marone, 1998; Scholz, 1998). When (a - b) is greater than 0, the fault exhibits velocity-strengthening (VS) behavior, which acts to inhibit seismic stick-slip events. Conversely, when (a - b) is less than 0, it displays velocity-weakening (VW) behavior. In VW faults, the stability of the slip behavior is governed by the system stiffness, k, and the critical stiffness, k (Rice & Ruina, 1983; Ruina, 1983), where

$$k_c = \frac{\sigma_n(b-a)}{D_c}. (4)$$

SONG AND MCLASKEY 2 of 16

The slip behavior is considered unstable when  $k/k_c < 1$  and stable when  $k/k_c > 1$ . Considering the stiffness of a fault embedded in a material with shear modulus G, the critical nucleation length,  $h^*$  is inversely proportional to the critical stiffness:

$$h^* = \frac{G}{k_c} = \frac{GD_c}{\sigma_n(b-a)} \tag{5}$$

An alternative expression of  $h^*$  contains the parameter  $R_b = (b - a)/b$  (Ampuero & Rubin, 2008; Rubin & Ampuero, 2005)

$$h_{\infty}^* = \frac{h^*}{\pi R_b} = \frac{bGD_c}{\pi \sigma_n (b - a)^2}.$$
 (6)

#### 3. Materials and Methods

## 3.1. Sample and Experimental Setup

Two PMMA blocks were loaded with the biaxial machine shown in Figure 1a and previously described in detail (Cebry & McLaskey, 2021; Mclaskey & Yamashita, 2017). In this study, the moving block has the dimensions of 760 by 203 by 38 mm in x, y, and z directions, respectively, and the stationary block has the dimensions of 790 by 152 by 38 in x, y, and z directions, respectively. The PMMA ( $G_{\rm PMMA\_dynamic} \approx 2$  GPa) is more compliant than granite rock ( $G_{\rm rock\_dynamic} \approx 30$  GPa) and is used for the experiments, so that, elastically, we can simulate ~11 m of rock (760 mm  $\times$   $G_{\rm rock\_dynamic}/G_{\rm PMMA\_dynamic}$ ). Normal stress was applied to the fault using four hydraulic cylinders and shear stress was applied with a fifth cylinder located at the forcing end (i.e., North, N). The opposite side of the sample is called the leading end (i.e., South, S).

#### 3.2. Sensors and Instrumentation

As depicted in Figure 1a, local fault slip was measured using eight eddy current sensors attached with hot glue, located at 100 mm intervals in the x-direction (E1–E8). Each eddy sensor measures the gap between a probe and a steel target at a resolution of  $\sim$ 0.15  $\mu$ m and 20 kHz sampling rate. To measure the local slip of the fault, the probes were attached to the stationary block and the steel targets were glued to the moving block. Four Piezoelectric sensors (Panametrics, V103) were mounted on the surface of the stationary block, situated 30 mm away from the fault in the y-direction, with a spacing of 200 mm in the x-direction (P1–P4). These piezoelectric sensors were capable of capturing ground motion in the z-direction of the PMMA blocks. The signal was continuously recorded at 20 kHz and also recorded in triggered mode at 2 MHz for 50-ms-long data blocks. The sample-average shear and normal stresses applied to the interface were calculated from hydraulic pressure measurements in the hydraulic cylinders.

#### 3.3. Initial Sample Preparation

The fault surfaces of the moving and stationary blocks were prepared by fly cutting in a mill to first make flat surfaces and then roughening them with 80 grit abrasive. Those blocks were then positioned in the biaxial machine, subjected to a normal stress  $\sigma_n = 16$  MPa, and sheared at ~3  $\mu$ m/s for 2.5 mm of slip. This shearing was repeated twice with realigned moving blocks. Finally, the fault surfaces of both blocks were washed with water.

#### 3.4. Teflon Surface Treatment

To prepare the heterogeneous fault sample, the entire fault area of both blocks was first covered with Teflon (Taegatech, PTFE tape, 0.813 mm (0.032 in) thickness and 50.8 mm (2 in) wide), affixed using cellophane tape on the top and bottom of the PMMA blocks. To prevent the two Teflon-covered PMMA surfaces from sticking together, plastic wrap (GLAD, Clingwrap) was placed between them. The assembly was then subjected to  $\sigma_n = 16$  MPa normal stress and sheared for 1 mm to adhere the Teflon to the PMMA, after which the Teflon layer was carefully removed on part of the fault to create the desired size of the bare PMMA patch to make a single asperity (Figures 1b and 1c). The prepared specimen was then placed in the testing machine, with plastic wrap inserted only at the Teflon patches.

SONG AND MCLASKEY 3 of 16

21699356, 2024, 4, Downloaded from https://agupuds.onlinelibrary.wiley.com/doi/10.1029/2023JB028509 by Cornell University, Wiley Online Library on [15/07/2024]. See the Terms

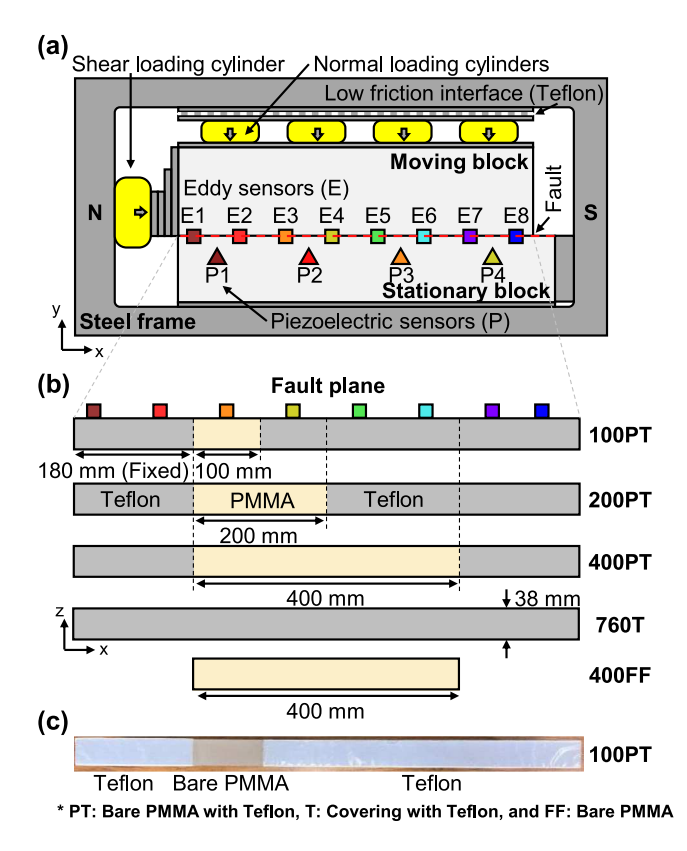


**Figure 1.** The biaxial experimental setup and various samples. (a) Schematic diagram of the biaxial apparatus showing the sensor locations and the moving and stationary PMMA blocks subjected to shear and normal stresses. (b) Side views showing the fault plane with the dimensions of the bare PMMA (velocity weakening) and Teflon (velocity strengthening) patches for different experimental configurations. (c) Photograph showing the Teflon on the moving block after experiment 100PT.

The friction properties of the Teflon/plastic wrap interface were determined from a sample where the entire fault area was Teflon/plastic wrap (760T in Figure 1b). Some evolution of friction (i.e., a run-in phase) was observed with cumulative slip, but properties stabilized after  $\sim$ 4 mm of slip to a VS behavior, as shown in Figure A1. We found  $(a-b)\approx 0.0025$  at  $\sigma_n=2$  MPa, and the interface became more velocity neutral with increasing  $\sigma_n$  such that  $(a-b)\approx 0.001$  at  $\sigma_n=16$  MPa. The friction coefficient derived from the sample-averaged shear and normal stresses of Teflon ranges from 0.05 to 0.08 (Figure A1c). In contrast, the friction coefficient for bare PMMA,  $\sim$ 0.7 is  $\sim$ 10 times higher compared to that of the Teflon patch.

## 3.5. Experimental Procedure

To promote consistent results, we conducted a run-in phase before all experiments involving Teflon (see details in Figure A1). After the desired  $\sigma_n$  was applied (ranging from 2 to 16 MPa), the sample was sheared for  $\sim$ 4 mm before recording data. All experiments were loaded with an electric pump (ReaXus LS-Class, TELEDYNE ISCO) at a constant long-term slip rate of  $\sim$ 3  $\mu$ m/s. To help distinguish between the effects of  $\sigma_n$  and any effects of cumulative wear of the interface, experiments with a given Teflon-PMMA geometry were conducted in the sequence: 4, 8, 2, and 16 MPa.

## **3.6.** Free Fault (400FF)

To directly compare our experiments with rupture contained by VS Teflon to a case with free end conditions, we also conducted experiments using a bare PMMA moving block of length 400 mm (400 FF) without Teflon covering the ends (Figure 1b). Thus, configuration 400 PT and 400 FF have the same asperity size L and the same  $h^*$ . For 400 FF, we attached four Eddy sensors and four Piezoelectric sensors to the block, utilizing the same sensor geometry as the 400PT setup.

SONG AND MCLASKEY 4 of 16

21699356, 2024, 4, Downloaded from https://agupubs.onlinelibrary.wiley.com/doi/10.1029/2023JB028509 by Cornell University, Wiley Online Library on [1507/2024]. See the Terms and Conditional Conditio

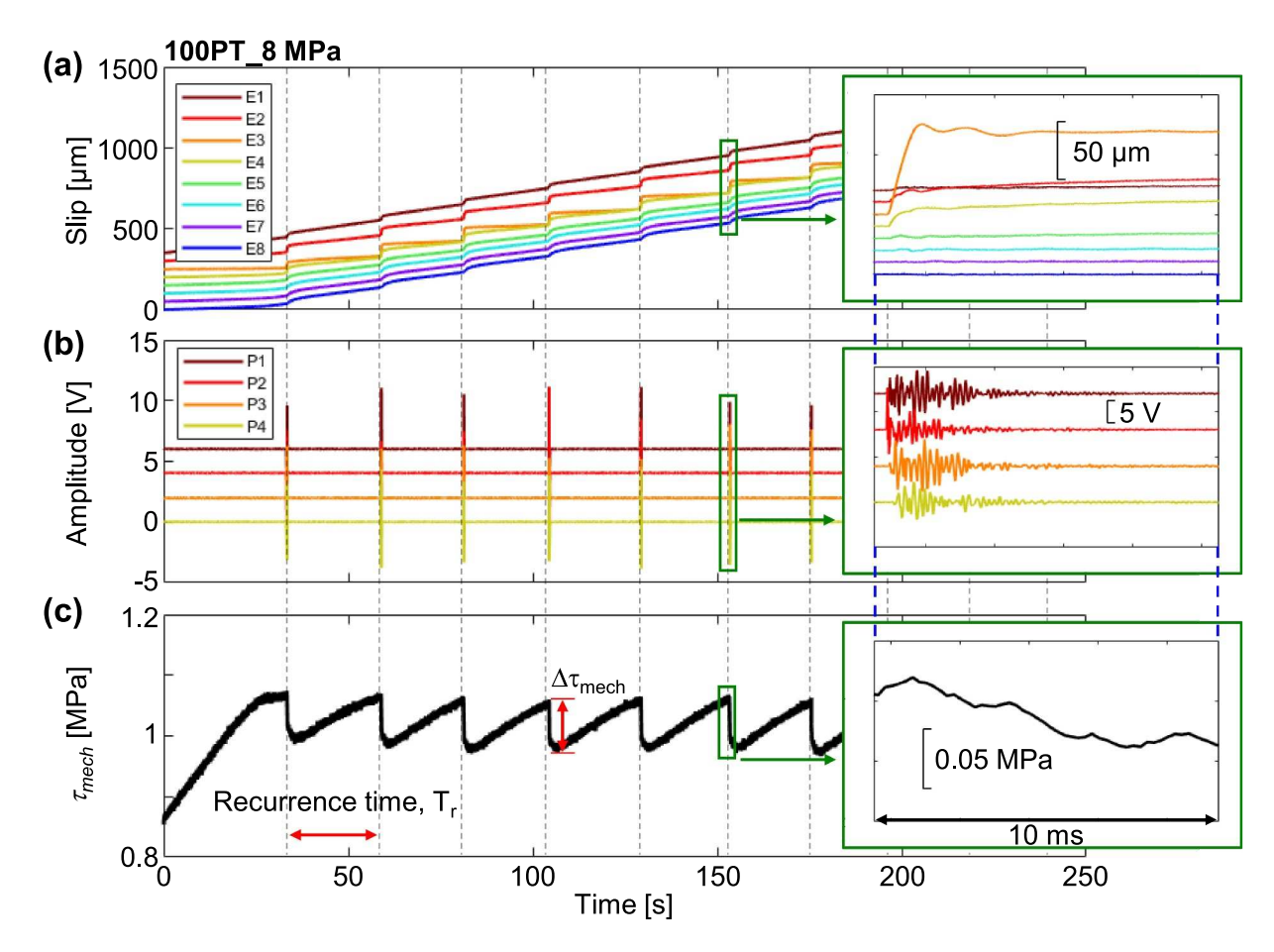


Figure 2. Representative behavior including (a) local fault slip, (b) acoustic signals, and (c) sample-average shear stress ( $\tau_{\rm mech}$ ) of 100PT at  $\sigma_n = 8$  MPa. The sudden drop of shear stress associated with a slip event is denoted  $\Delta \tau_{\rm mech}$ . The stick-slip events are indicated by dotted vertical lines and the time interval between events is referred to as the recurrence time,  $T_r$ .

## 3.7. Digital Image Correlation (DIC)

The Digital Image Correlation (DIC) technique was adopted to measure strain along the fault (Figure S1 in Supporting Information S1). Red speckles were painted on a white background painted on the surface of the moving block. Images were taken using a camera (Nikon, D850) with a resolution of ~93 µm/pixel. A reference image (i.e., undeformed image) was taken while the sample was at  $\sigma_n = \sim 0.1$  MPa and deformed images were captured close to the peak shear stress, measured from the hydraulic pressure in the shear loading cylinder. 2D cross-correlation was used to match speckles between the reference and deformed images. This was used to create a deformation field and strain fields were derived from the deformation (see details in Figures S1b and S1c in Supporting Information S1). The shear and normal stresses were calculated using Hook's law for plane strain, assuming Young's modulus,  $E_{\rm PMMA\_static} = 2.3$  GPa and Poisson's ratio,  $\nu = 0.3$ . We achieved sub-pixel resolution by upsampling by a factor of 20. Assuming a minimum resolvable displacement of  $\pm 4.7$  µm/pixel, we estimate a minimum resolvable normal stress and shear stress of  $\pm 0.6$  and  $\pm 0.1$  MPa, respectively (Figure S1 in Supporting Information S1). These values are consistent with Cebry et al. (2023) who conducted DIC analysis with similar parameters.

## 4. Results

## 4.1. Example of Slip Behavior

We first present an example of a typical stick-slip sequence in order to define parameters and illustrate the general results. Figures 2a–2c show the slip, ground motion, and the sample-average shear stress ( $\tau_{\rm mech}$ ) derived from hydraulic pressure in the shear cylinder from the 100 PT experiment at  $\sigma_n = 8$  MPa. Note that  $\tau_{\rm mech}$  is computed by

SONG AND MCLASKEY 5 of 16

2169936, 2024, 4, Downloaded from https://aguputs.onlinelibrary.wiley.com/doi/10.1029/2023JB028509 by Cornell University, Wiley Online Library on [15/07/2024]. See

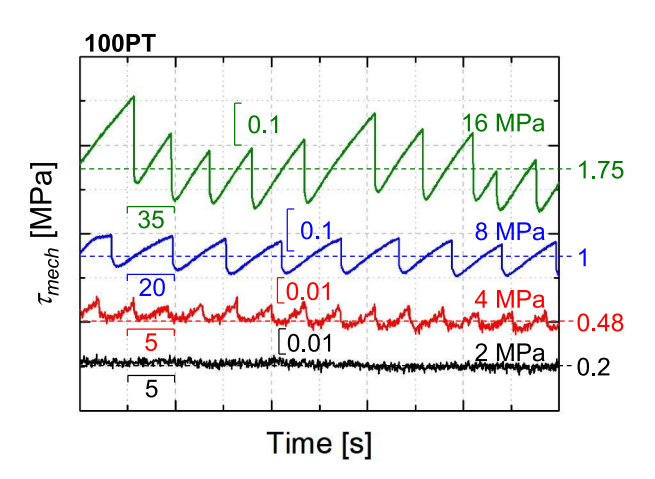


**Figure 3.** The  $\tau_{\rm mech}$  with time of 100PT under different normal stresses. Note the different time and amplitude scalebars and reference shear stress (dotted line) for each test. As the normal stress increases,  $L/h^*$  increases, and the sample behavior transitions from steady sliding (2 MPa) to periodic slow (4 MPa) and fast (8 MPa) slip events, to aperiodic sequences (16 MPa).

dividing the force supplied by the shear cylinder by the fault area  $(760 \times 38 \text{ mm})$ . Stick-slip events are defined as the sudden drop of shear stress ( $\Delta \tau_{\text{mech}}$ ) accompanied by rapid fault movement (Figures 2a and 2c). Notably, the sensor E3 moves more than other sensors, as it is located in the bare PMMA region (inset in Figure 2a). The drop in  $\Delta \tau_{\text{mech}}$  does not correspond to the abrupt slip of sensor E3 (inset in Figure 2c). It decreases more gradually with time due to accelerated slow slip near the forcing end (E1). The period between stick-slip events is referred to as the interseismic period and the recurrence time  $(T_r)$  denotes the time between successive stick-slip events. Ground motion during each stick-slip event is captured by four piezoelectric sensors (e.g., P1, P2, P3, and P4) as shown in Figure 2b. The sensor P2 first detects the ground motions (inset in Figure 2b) since it is closest to the bare PMMA region (Figure 1a).

Figure 3 presents the evolution of the  $\tau_{\rm mech}$  over time for 100 PT at 2, 4, 8, and 16 MPa normal stresses. Note that the scale of time and shear stress is different for each normal stress level. At 2 MPa normal stress, the shear stress remains constant at ~0.2 MPa, without showing any stick-slip events. In contrast, at 4 MPa normal stress, it starts to show slow slip events. The  $T_r$  and  $\Delta \tau_{\rm mech}$  increase with increasing normal stress. Notably, the sample undergoes regular and periodic slip cycles at  $\sigma_n = 4$  and 8 MPa, whereas the sample behavior is non-periodic and more variable at  $\sigma_n = 16$  MPa.

Figures 4a–4c present examples of the spatial distribution of slip over five consecutive stick-slip cycles. Closely spaced pink and purple bands indicate slower slip while widely spaced pink and purple bands indicate faster slip. The black lines show the slip distribution plotted every 100  $\mu$ s to show the rapid slip during stick-slip events. A low normal stress and a small bare PMMA patch (e.g., 200 PT with 4 MPa normal stress) show periodic slip (Figure 4a). However, at higher normal stress (16 MPa), Figures 4b and 4c show non-periodic sequences.

Figures 4d–4f show the slip rate derived from the same Eddy current sensor data shown in Figures 4a–4c. The loading rate at the forcing end (E1) matches our applied loading rate and remains constant at  $\sim$ 3  $\mu$ m/s (yellow dotted line) during the interseismic period regardless of the normal stress and PMMA patch sizes. The shear loading rate is known to influence the slip nucleation process (Guérin-Marthe et al., 2019; Kaneko et al., 2016; Xu et al., 2018), so this constant slip rate at E1 helps ensure a constant loading rate on the bare PMMA patch and more consistent conditions for the nucleation process. During the interseismic period, the slip rate in the bare PMMA region (e.g., E3 and E4) is lower compared to the Teflon region (Figure 4d) but gradually increases before each stick-slip event. During the slip event, it reaches  $\sim$ 100 mm/s. For experiments at higher normal stress, the slip rate in the bare PMMA region is even lower during the interseismic period (Figure 4e). In the 400 PT experiment, it is clear that interseismic slip rates are variable across the VW asperity, with the lowest slip rate occurring closer to the center of the bare PMMA region, at E4 (Figure 4f).

SONG AND MCLASKEY 6 of 16

21699356, 2024, 4, Downloaded from https://agupubs.onlinclibrary.wiley.com/doi/10.1029/2023JB028599 by Cornell University, Wiley Online Library on [15/07/2024]. See the Terms and Conditions (https://onlinelibrary.wiley.com/fer

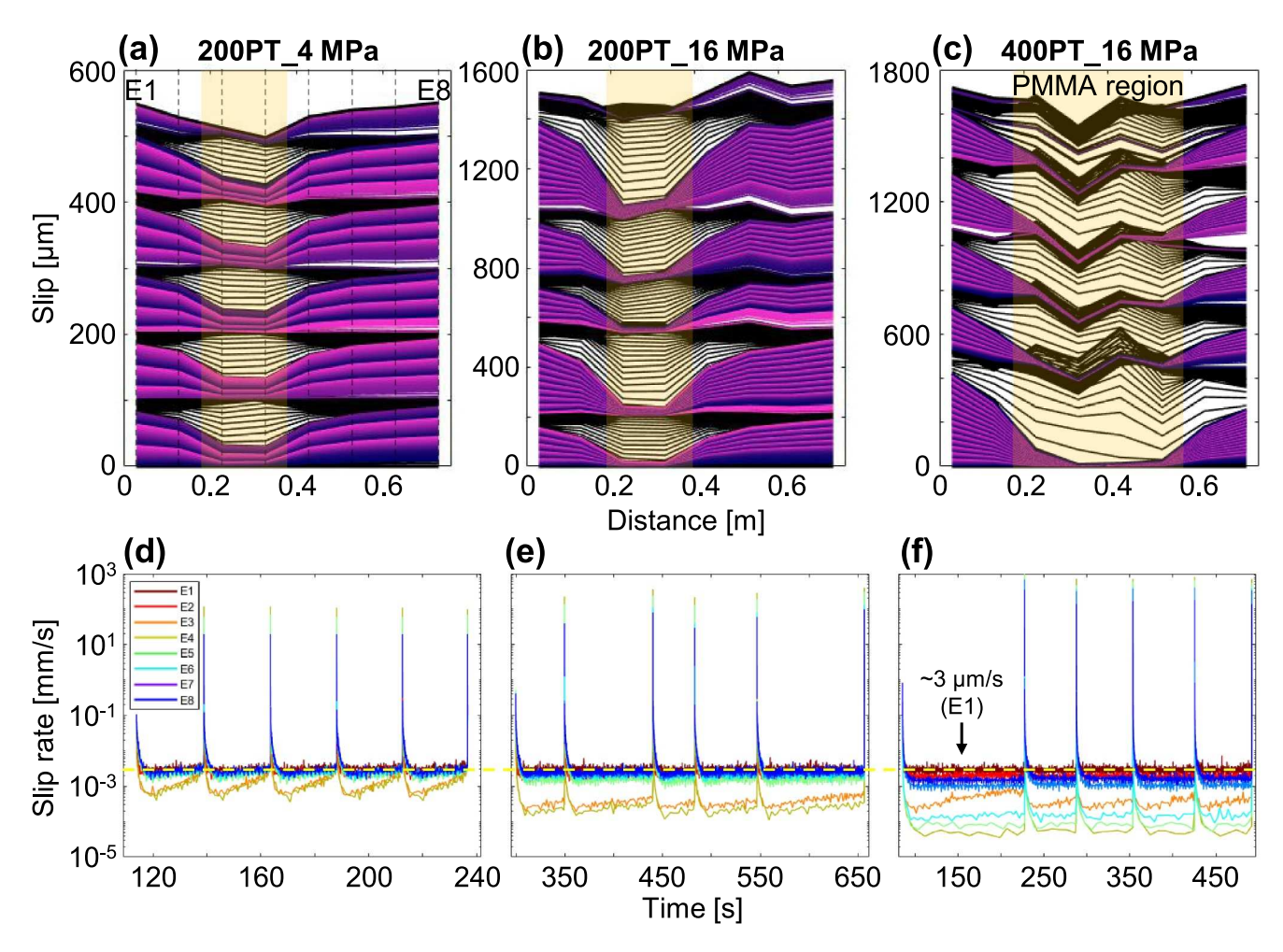


**Figure 4.** Accumulated slip along the fault for five stick-slip cycles. (a–c) The distribution of slip along the fault from E1 to E8. For the pink and purple lines, a line is plotted every 100 ms with a 10 s color cycle. The black lines show slip distribution plotted every 100 μs during a slip event. The yellow shaded area indicates the location of the PMMA patch. Experiment names and  $σ_n$  levels are indicated above each plot. (d–f) The slip rate over the five stick-slip cycles, derived from the same data as in panels (a–c). Stick-slip events show up as spikes of high slip rate. During the interseismic period, the slip rate near the forcing end (E1) remains constant at the driving rate of ~3 μm/s (yellow dotted line), while the slip rate on the asperity is lower, indicating relative locking and accumulation of slip deficit.

#### 4.2. Maximum Slip Rate

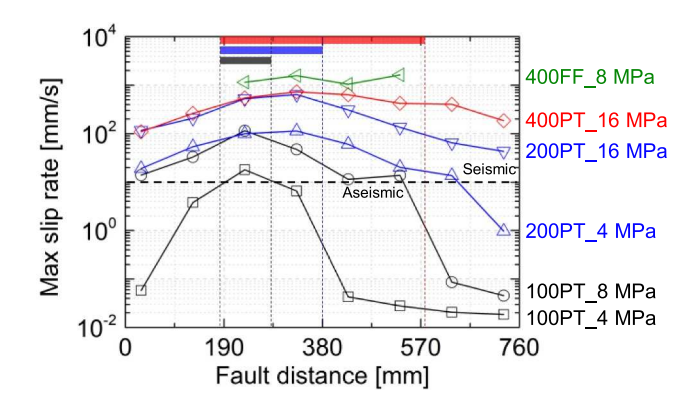
Figure 5 shows the maximum slip rate of each Eddy sensor along the fault throughout the entire stick-slip cycle. Each data point shows the average maximum slip rate based on 6 to 12 stick-slip events. Following previous work, we set a boundary of 10 mm/s to differentiate between seismic (or dynamic) slip and aseismic slip (McLaskey, 2019; Wu & McLaskey, 2019). The distribution of the maximum slip rate exhibits a symmetric configuration, with its peak at the center of the bare PMMA patch. For the 100 PT\_4 MPa, seismic slip is observed within the bare PMMA region, while the Teflon patch shows aseismic slip. As the normal stress increases or the size of the bare PMMA patch increases, seismic slip extends further and further into the Teflon region. However, even when the entire fault slips at seismic rates, the Teflon regions near the sample ends are still limiting the slip rate. This contrasts with the experiment with free ends and no Teflon, 400 FF\_8 MPa, which shows consistent slip rates across the entire fault, or even increased slip rates at the sample ends.

Figure 6a illustrates the maximum slip rate measured anywhere on the fault,  $\dot{D}_{max}$ , during each stick-slip event and how this changes as a function of normal stress. At 2 MPa normal stress, both 100 and 200 PT exhibit aseismic slow slip events, with  $\dot{D}_{max}$  of ~20  $\mu$ m/s (still far larger than the applied loading rate of 3  $\mu$ m/s). The results demonstrate an increase of the  $\dot{D}_{max}$  as the normal stress increases.

SONG AND MCLASKEY 7 of 16

21699356, 2024, 4, Downloaded from https://agupubs.onlin

library.wiley.com/doi/10.1029/2023JB028509 by Cornell University, Wiley Online Library on [15/07/2024]. See



**Figure 5.** The maximum slip rate of each sensor during the stick-slip event with respect to the fault distance. Note that black, blue, and red shaded areas present the bare PMMA region in 100, 200, and 400 PT, respectively.

Figure 6b shows the same data plotted against  $L/h^*$ . The  $\dot{D}_{max}$  roughly collapses to a single curve. In this study, we only controlled the dimensions of the asperity while keeping the frictional properties of the material constant. Therefore, we assumed that  $G_{\rm dynamic}$ ,  $D_c$ , and (b-a) remain the same and, therefore,  $h^*$  is only influenced by the normal stress (Equation 5). From previous studies of the friction parameters of glassy polymers, we assume  $(b-a)\approx 0.005$  and  $D_c\approx 0.35~\mu m$  (Lu, 2009), such that  $G_{\rm dynamic}\cdot D_c/(b-a)\approx 140~mm$  MPa. From this, we find that the transition from seismic to aseismic slip occurs at  $L/h^*\approx 2.8$ . With increasing  $L/h^*$ ,  $\dot{D}_{max}$  gradually increases from ~20 mm/s to ~1 m/s at  $L/h^*\approx 45$ . Figure 6b also compares our experimental results to the numerical simulations of Barbot (2019) (green arrow). Variations in the geometry and boundary conditions of Barbot (2019)'s model (such as anti-plane strain vs. 2D fault) resulted in variations in the values of  $L/h^*$  at the boundary between seismic and aseismic slip; however, the general trend in  $\dot{D}_{max}$  remains similar to our experimental findings.

#### 4.3. Variation in Recurrence Time and Seismic Moment With $L/h^*$

Figure 7a depicts the recurrence time,  $T_r$ , against  $L/h^*$  for the same experiments as shown in Figure 6, except experiments that exhibit aseismic slip are not plotted. As  $L/h^*$  increases, the recurrence time increases and the variation in recurrence time also increases. The inset in Figure 7a shows the normalized standard deviation (SD) of  $T_r$  (Norm\_SD) defined, for each sequence of slip events, as the SD of the  $T_r$  divided by the average  $T_r$ . For  $L/h^* < 6$ , the Norm\_SD is less than  $\sim$ 0.06, indicating highly periodic slip behavior. However, for  $L/h^* > 10$ , the Norm\_SD increases up to 0.75 indicating non-periodic slip. Based on these results, we denote the transition from

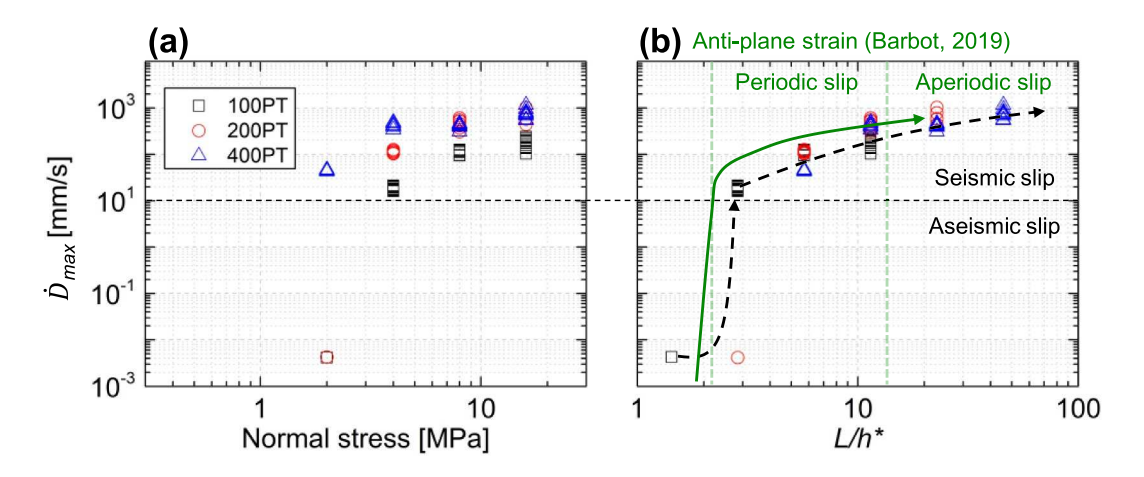


**Figure 6.** Maximum slip rate at the PMMA patch with various PMMA patch sizes, showing its relationship with (a) the normal stress and (b)  $L/h^*$ . Each symbol is a slip event. We assumed that  $h^*$  is 140 mm at 1 MPa. We compared our results (symbols and black dashed lines) to those from the anti-plane strain numerical simulation results from Barbot (2019) in green.

SONG AND MCLASKEY 8 of 16

21699356, 2024, 4, Downloaded from https://agupubs.onlinelibrary.wiley.com/doi/10.1029/2023JB028509 by Cornell University, Wiley Online Library on [15/07/2024]. See

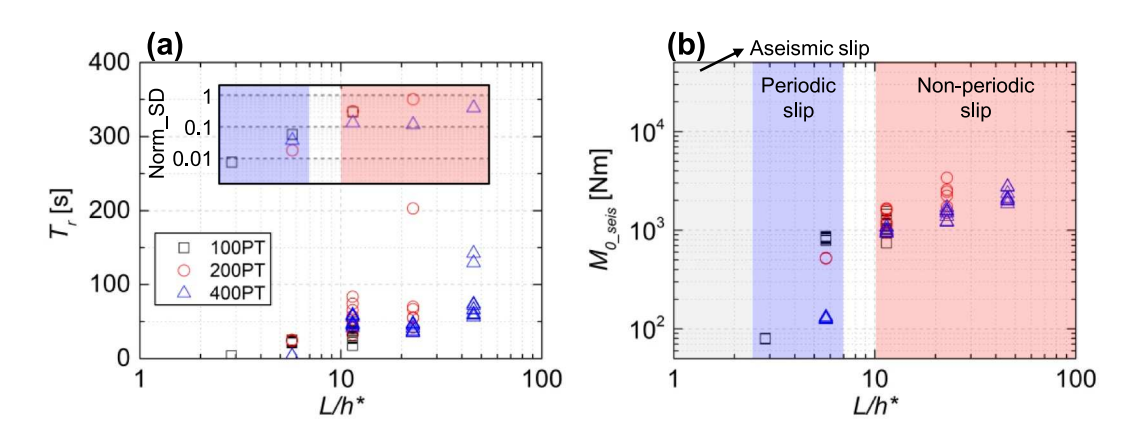


Figure 7. (a) Recurrence time against  $L/h^*$  for each stick-slip event in all tests. Inset shows the standard deviation of recurrence time for events in each test. (b) Seismic moment (from spectra of recorded ground motions) against the  $L/h^*$  for each stick-slip event. The area is divided into three regions: as eismic slip (gray shaded area with  $L/h^* < 2$ ), periodic slip (blue shaded area with  $2 < L/h^* < 6$ ), and non-periodic slip (red shaded area with  $L/h^* > 10$ ).

periodic to non-periodic slip behavior at  $L/h^* \approx 8$ , although the Norm\_SD results suggest that this specific transition might be arbitrary.

Figure 7b shows how the seismic moment,  $M_{0\_seis}$ , obtained from the piezoelectric sensors, varies with  $L/h^*$ .  $M_{0\_seis}$  is calibrated using a ball drop empirical Green's function (see details in Figure S2 in Supporting Information S1). Note the large reduction in seismic moment observed at low  $L/h^*$ , close to the boundary. In the "non-periodic slip" region, we observe a greater variability in event sizes during the same test.

## 4.4. Slip Behavior of the Free Fault Compared to the Contained Fault

To further investigate the effects of rupture containment with a VS region, we directly compared slip behaviors between a contained fault (CF, 400 PT\_8 MPa) and a free fault (FF, 400 FF\_8 MPa) with the same L and same  $h^*$ , described in Table 1. Values presented in the table are the average of many stick-slip events, along with minimum and maximum values in parentheses. A is the fault area.  $\sigma_{n_{\rm max}}$  and  $\tau_{\rm mech_{\rm max}}$  are the maximum sample-average normal and shear stresses, respectively, just prior to a slip event, derived from hydraulic pressure measurements.  $F_{\rm max} = \tau_{\rm mech_{\rm max}} \cdot A$  is the maximum sample-average shear force. The parameters  $T_r$  and  $\Delta \tau_{\rm mech}$  were described previously.  $D_{\rm avg}$  dynamic is the average dynamic slip expressed as

$$D_{\text{avg\_dynamic}} = \frac{1}{n} \sum_{i=1}^{n} D_{i\_dynamic} = \frac{1}{n} \sum_{i=1}^{n} \int_{t_1}^{t_2} \delta_i(t) dt,$$
 (7)

where  $\delta_i$  is the slip measured with the *i*th eddy current sensor when the slip rate exceeds 10 mm/s for 0.1 ms duration and n=8 is the number of eddy current sensors,  $t_1$  is when  $d\delta/dt > 10$  mm/s, and  $t_2$  is when  $d\delta/dt < 10$  mm/s. The  $M_0$  mech is modified from the standard  $M_0 = GAD$  expression (Aki, 1966), to be

$$M_{0\_\text{mech}} = G_{\text{dynamic}} W \int_0^{0.76 \text{ m}} D_{\text{dynamic}}(x) dx, \tag{8}$$

**Table 1**Comparison Between Free Fault (400 FF\_8 MPa) Conditions and Contained Fault (400 PT\_8 MPa)

	$A \text{ (cm}^2)$	$\sigma_{n_{-}\mathrm{max}}$ (MPa)	$\tau_{\mathrm{mech\_max}}$ (MPa)	$F_{\text{max}}$ (kN)	$T_r(s)$	$\Delta \tau_{\rm mech}$ (MPa)	$D_{\text{avg\_dynamic}} (\mu \text{m})$	$M_{0\_{\rm mech}}$ (kN m)	$M_{0_{\text{seis}}}$ (kN m)
FF	152.4	8.2 (8.0-8.3)	5.7 (5.4–5.9)	87 (83–90)	259 (236–280)	3.1 (2.6–3.4)	1,119 (910–1,274)	39 (32–45)	3.4 (2.0–3.8)
CF	289.6	7.8 (7.7–7.8)	2.6 (2.6–2.7)	77 (76–78)	41 (35–47)	0.36 (0.3-0.4)	103 (71–123)	6.2 (4.3–7.3)	1.5 (1.2–1.7)
FF/CF	0.53	1.1	2.2	1.1	6.4	8.6	10.8	6.3	2.3

SONG AND MCLASKEY 9 of 16

21699356, 2024, 4, Downloaded from https://agupubs.onlinelibrary.wiley.com/doi/10.1029/2023JB028509 by Cornell University, Wiley Online Library on [15/07/2024]. See the Terms

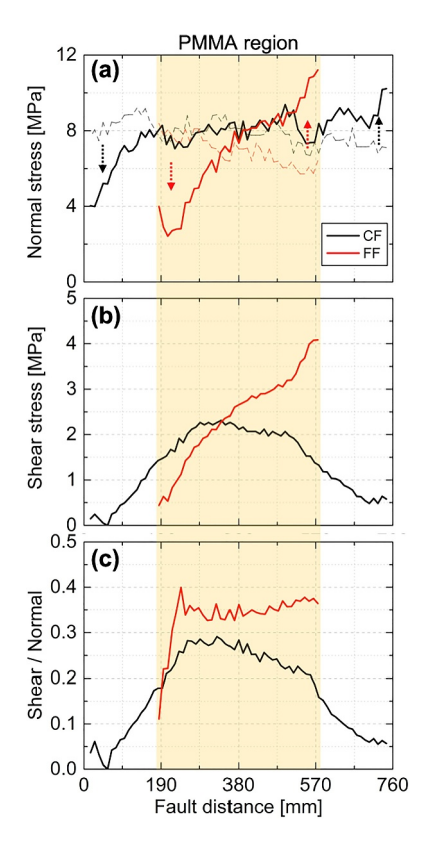


**Figure 8.** Stress distributions obtained by Digital Image Correlation under 8 MPa normal stress. (a) Normal stress distribution at  $\tau_{\text{mech\_max}}$ . Note that the dotted lines are the normal stress when only the normal stress was applied without shear stress. (b) Shear stress distribution at the  $\tau_{\text{mech\_max}}$ . (c) Friction coefficient of shear and normal stresses. The yellow shaded area is the bare PMMA region.

where W = 38 mm is the sample thickness and  $D_{\rm dynamic}(x)$  is the distribution of dynamic slip derived from the interpolation of  $D_{i\_{\rm dynamic}}$ .  $M_{0\_{\rm seis}}$ , is determined from piezoelectric sensor measurements, as described in Figure S2 in Supporting Information S1. Note that we analyzed 5 and 9 consecutive stick-slip events in FF and CF, respectively.

From Table 1, significant differences are observed despite them having the same VW patch size and  $h^*$ . Specifically, the mechanical properties such as  $T_r$ ,  $\Delta \tau_{\rm mech}$ ,  $D_{\rm avg\_dynamic}$ , and  $M_{0\_{\rm mech}}$  in the FF are found to be 6–11 times higher compared to the CF. However, the observed difference in  $M_{0\_{\rm seis}}$  is only 2.3 times.

Figure 8 shows the DIC results of both the CF and the FF (see method in Section 3.7). In addition to the reference image, deformed images were captured when only normal stress was applied to the block (dashed line in Figure 8a) and at  $\tau_{\text{mech\_max}}$ , prior to the occurrence of a stick-slip event. When  $\tau_{\text{mech\_max}}$  was applied, as depicted by the solid lines, the normal stress decreased near the forcing end and increased at the leading end due to the shear-force-induced torque in this single direct shear biaxial setup. Nevertheless, in the CF case, a nearly constant normal stress is observed within a bare PMMA region since it is sufficiently from the sample ends. The shear stress distribution in the FF resembles the normal stress distribution because the friction properties are uniform along the fault (Figure 8b). However, the shear stress at both ends in the CF is comparably lower than in the middle because the Teflon has a lower friction coefficient than the bare PMMA interface. Although the center of the sample involves the same bare PMMA region, the stress levels are lower in the CF case than in FF (Figure 8c).

## 5. Discussion

In these experiments, instead of employing a sample with uniform VW properties, we introduced Teflon tape as VS patches at the fault ends to establish a more CF rupture condition (Figure 1). This experimental condition corresponds more closely to the condition of previous numerical simulations (Barbot, 2019; Cattania, 2019; Chen

SONG AND MCLASKEY 10 of 16

& Lapusta, 2009; Kaneko & Lapusta, 2008; Lapusta & Liu, 2009; Lapusta & Rice, 2003; Lui & Lapusta, 2016, 2018). Our setup is somewhat similar to experimental studies that utilized fault gouge, which is effective for the confinement of the rupture (Bedford et al., 2022; Buijze et al., 2021); however, differential compaction of different gouge materials can produce heterogeneous normal stress, and we have shown that the normal stress is relatively uniform within the VW patch in our experiments (Figure 8a). We altered the size of the bare PMMA region and normal stress to systematically control  $L/h^*$  on the fault system. Our observations closely match numerical studies and highlight a range of slip behaviors depending on  $L/h^*$ , ranging from assismic slip at low  $L/h^*$  to non-periodic slip at high  $L/h^*$ . Also, we found significant differences in slip behavior, depending on different fault constraint conditions (e.g., FF and CF conditions) even within the same  $L/h^*$  values.

#### 5.1. Various Slip Behaviors as a Function of $L/h^*$

Our results show a distinct transition in behavior (Transition 1) from assismic slip at low  $L/h^*$  to seismic slip at higher  $L/h^*$  and another, less-well-defined boundary (Transition 2) at higher  $L/h^*$  where periodic slip events become more aperiodic. In previous laboratory studies, Transition 1 was investigated by changing the stiffness ratio of the system,  $k/k_c$  (see Section 2) within the range of  $\sim 0.5 - \sim 1.1$  which can be converted to  $0.9 \le L/h^* \le 2$ since  $k/k = L/h^*$  (Leeman et al., 2016; Scuderi et al., 2016; Veedu et al., 2020). All of those studies employed homogeneous fault properties with free end conditions. Transition 1 was found to occur at  $L/h^* \approx 1-1.3$ , which is similar to our observation of  $L/h^* \approx 2$  despite differences in boundary conditions between previous experiments and our contained ruptures. Note that all of these quantitative estimates of Transition 1 are limited by our poor ability to quantitatively estimate  $h^*$  since direct measurement of friction parameters (b-a) and  $D_c$  for bare PMMA are not achievable in our experimental setup. Inaccurate  $h^*$  would simply shift the data along the xaxis in Figures 6b and 7, but would not affect the general trends. Near Transition 1, all studies found sharp changes in  $\dot{D}_{max}$  in response to minor changes in  $L/h^*$ . For example, we find  $\dot{D}_{max} \sim 4 \, \mu \text{m/s}$  at  $L/h^* = 1.4$  and ~10 mm/s at  $L/h^* = 2.8$  (Figure 6b). For Transition 2, a bifurcation in slip behavior (e.g., alternation of slow and fast slips) has been reported (Mei et al., 2022; Veedu et al., 2020) under a narrow range of conditions. In addition to  $L/h^*$ , Luo and Ampuero (2018) found the relative strength parameter,  $\alpha = (b-a)_{VW}/(a-b)_{VS}$ , to be an important factor in determining slip behavior. We assumed that  $(b-a)_{VW}$  for bare PMMA remains constant regardless of normal stress, while  $(a - b)_{VS}$  for Teflon decreases as normal stress increases (Figure A1). As a result,  $\alpha$  ranges from 1.9 to 3.3 at  $L/h^* = 5.6$ , placing it within the P-instability region. In this area of parameter space, the limited variation of  $\alpha$  does not significantly alter the slip behavior in comparison to changes in  $L/h^*$ .

Fault stability has also been investigated using numerical simulations, which commonly model a single VW asperity bounded by the VS materials (Barbot, 2019; Cattania, 2019). Cattania (2019) reported results in terms of  $h_{\infty}^*$  and used a=0.015 and b=0.02 ( $R_b=0.25$ ) for the analysis, which results in  $h^*\approx 0.8$   $h_{\infty}^*$  (Equation 6). That study reported Transition 1 at  $L/h^*\approx 0.8$  and Transition 2 near  $L/h^*\sim 5$ , with increasing numbers of earthquakes per supercycle progressively increasing for  $L/h^*\geq -5$  (Cattania, 2019). Barbot (2019) found Transition 1 at  $2 < L/h^* < 6$ , depending on boundary conditions, and Transition 2 at  $L/h^*\approx 6$ , but this varied depending on  $R_b$  (Barbot, 2019). The above numerical results are in reasonable agreement with our observations (Transition 1 at  $L/h^*\approx 2$  and Transition 2 at  $L/h^*\approx 8$ ). The two transitions are evident across both numerical and experimental studies, and this suggests that  $L/h^*$  is a reliable parameter to determine a sample behavior.

## 5.2. Contained Rupture Versus Free Fault Rupture

In this Section, we discuss the effect of slip behavior between the CF, where a VW patch is contained by VS material and the FF, where the VW patch is bounded by free surfaces. We made the same area of the bare PMMA for both the FF and CF tests. In terms of strength, we observed that  $F_{\rm max}$  is 13% larger for FF while the normal stress is only 5% larger (Table 1). This shows that not only did the Teflon patches added in the CF case provide minimal shear resistance, they acted to weaken the surrounding VW fault sections. The DIC results also demonstrate this effect when examining the ratio of local shear stress to normal stress in the bare PMMA region: FF condition exhibits an average value of  $\sim$ 0.35, whereas the CF condition has a lower average value of  $\sim$ 0.25 (Figure 8c). We also found that the sample-average friction coefficient in these heterogeneous tests is generally comparable to or slightly less than the area-averaged mixture of the friction coefficients of bare

SONG AND MCLASKEY 11 of 16

PMMA (0.7) and Teflon ( $\sim$ 0.07). Thus, the addition of the weak VS material effectively weakened the nearby VW material. This can be at least partially explained by the sliding during the interseismic period. In the FF case, the entire fault remains locked during the interseismic period (Figure S3 in Supporting Information S1), whereas in the CF case, the VW region creeps at 0.06–0.6  $\mu$ m/s. Numerical simulations (Chen & Lapusta, 2009) have also shown how creep in the VS region can penetrate into the VW region and "erode" the asperity and mitigate the accumulation of shear stress relative to areas that are fully locked. In natural faults, VW gouges (e.g., Quartz and Calcite) exhibit friction coefficient of  $\sim$ 0.7, while VS gouges (e.g., Clay and Talc) exhibit friction coefficient of  $\sim$ 0.2 (Bedford et al., 2022; Giorgetti et al., 2015). The friction coefficients of those natural materials are similar to those of PMMA and Teflon, thereby implying that similar asperity erosion patterns could be found in natural faults.

We note that the local friction coefficient estimated by DIC ( $\mu_{\rm DIC}$ ) is significantly lower than the sample-average friction coefficient ( $\mu$ ) estimated from the hydraulic pressure measurements. For example, the 400 FF\_8 MPa experiment produced  $\mu_{\rm DIC} \approx 0.4$  (Figure 8c) while  $\mu \approx 0.7$  (Table 1). Our estimate of  $\mu$  is a slight overestimate of the true friction coefficient on the fault,  $\mu_{\rm fault}$ , due to the contribution from the Low Friction Interface (LFI, see Figure 1a) which likely has a friction coefficient  $\mu_{\rm LFI} \approx 0.02$  between Steel and Teflon (Dieterich & Kilgore, 1994), the sample-average friction coefficient of the fault ( $\mu_{\rm fault} \approx 0.68 = \mu - \mu_{\rm LFI}$ ). Additionally,  $\mu_{\rm DIC}$  might be an underestimate since the measurements are made 20 mm from the fault (Figure S1 in Supporting Information S1) and we found that the measured shear strain decreases with increasing distance from the fault, especially near the forcing end of the sample. However, these effects don't seem to explain the large differences between  $\mu_{\rm DIC} \approx 0.4$  and  $\mu \approx 0.7$ . Despite this concern, our observations consistently show that the fault is weaker in the CF configuration than in the FF configuration.

The mechanical properties during slip events such as  $\Delta \tau_{\rm mech}$  and  $D_{\rm avg\_dynamic}$  are 8–10 times higher in the FF experiment compared to the CF. In this case, the Teflon appears to serve a dual purpose: it weakens the fault, as described above, and it also acts to arrest or decelerate slip during slip events by providing increased frictional resistance as the slip rate increases. Consequently, the presence of Teflon at both ends in the CF condition helps to reduce the amount of slip and the amount of  $\Delta \tau_{\rm mech}$  during slip events.

## 5.3. Rapid Slip in VS Regions Causes Imperfect Containment

As shown in Figures 4a-4c, the dynamic slip, (>10 mm/s) was primarily found in the bare PMMA region, but dynamic slip also extended into the VS patches. This is more evident in Figure 5, which delineates the  $\dot{D}_{max}$  along the fault distance. At small  $L/h^*$  (i.e., 100 PT\_4 MPa) seismic slip is confined to the bare PMMA region, but with increasing  $L/h^*$ , the slip rate in the Teflon patches increases even to seismic slip rates (>10 mm/s). Although we used Teflon to contain the rupture within the sample, it was not fully contained. Nevertheless, the presence of Teflon decelerated the slip in the region where it was applied. In contrast, in the FF condition, the slip rate can remain constant or even increase when it approaches the ends of the fault (see Figure 4 in Wu and McLaskey (2019) or Figure 5 in this study). In numerical simulations, it is also common to observe dynamic slip in VS regions next to VW regions, and the extent of dynamic slip in VS areas increases with an increase of  $L/h^*$  (Barbot, 2019; Cattania, 2019; Chen & Lapusta, 2009; Lapusta & Liu, 2009; Lui & Lapusta, 2016, 2018).

#### 5.4. Comparison of Mechanical Moment and Seismic Moment

We calculated  $M_{0\_mech}$  derived from mechanical measurements (Equation 8) and compared it to  $M_{0\_seis}$  based on ground motions detected with the piezoelectric measurements. The ratio of  $M_{0\_mech}/M_{0\_seis}$  was 11.5 and 4.1 for the FF and CF conditions, respectively, reported in Table 1. Thus, the mechanical moment overestimated seismic moment in both cases, but particularly in the FF condition, indicating that the efficiency of seismic wave radiation with respect to the amount of slip was lower in the FF condition compared to the CF condition. This may be attributed to the CF condition inducing more abrupt variations in slip rate, which could enhance wave radiation efficiency with respect to the slip. Our results are consistent with those of Wu and McLaskey (2019) who found the  $M_{0\_mech}/M_{0\_seis} \sim 10$  for complete rupture of a 3-m granite sample (i.e., FF conditions) and generally smaller values (1.5–4) for contained ruptures (i.e., CF rupture). Equation 8 is derived from a case where fault slip is zero over the entire perimeter of the rupture region. For the FF, the shear modulus G should be replaced in some way, by the effectively lower stiffness that the rupture feels from the

SONG AND MCLASKEY 12 of 16

## Journal of Geophysical Research: Solid Earth

loading apparatus compared to the case of completely contained rupture. When the rupture approaches a truly CF condition,  $M_{0 \text{ mech}}/M_{0 \text{ seis}}$  should approach unity.

The presence of the VS material on the fault ends does not guarantee a perfect CF condition, it is a closer approximation to the expected conditions of natural earthquakes than FF conditions, and this affects both the frictional behavior and seismic energy release. We encourage researchers to adopt the Teflon surface treatment since it can help contain the rupture and reduce edge effects associated with the free surfaces at the ends of the sample. It also facilitates a more homogeneous normal stress distribution within the VW patch simply because it moves the VW patch away from the sample ends where nonuniform normal stress is common.

## 6. Conclusions

We performed biaxial experiments on a 760 mm PMMA sample and created contained rupture using a Teflon surface treatment to make a VS barrier. We varied both the size of the bare PMMA region (L) and the normal stress on the sample to study the various slip behaviors in relation to  $L/h^*$ , which ranged from 1.4 to 45 in our experiments. Similar to previous studies, we observed behavioral changes with increasing  $L/h^*$  going from aseismic slip to periodic slip to non-periodic slip. These changes were also accompanied by an increase in maximum slip velocity during the slip events. The fact that similar behavior is observed in a variety of numerical simulations and previous laboratory experiments, indicates that  $L/h^*$  is one of the most robust metrics for classifying the behavior of relatively isolated VW fault sections, even under somewhat varied boundary conditions.

Experimentally, the Teflon surface treatment proposed here offers a relatively simple method for containing laboratory earthquake ruptures. This practice moves seismic slip away from the sample ends, where a nonuniform distribution of normal stress often occurs during standard direct shear experiments. This promotes a more uniform normal stress distribution on the VW patch, which more closely aligns with the conditions observed in numerical studies. Teflon on the fault ends also reduces the amplification of slip velocity that occurs when a dynamic rupture meets a free surface, and effect that is not expected for natural earthquakes whose ruptures are contained within the earth. By comparing the measured fault slip to the seismic moment calculated from measured ground motions, we found that uncontained ruptures associated with slip all the way to the free surfaces did not radiate seismic waves as efficiently, with respect to the slip, as did contained ruptures. The VS regions near the sample ends slowed down dynamic rupture, even if it did not always stop it completely, and this produced earthquake ruptures whose seismically estimated moment more closely matched their mechanically estimated moment.

Our experiments also provide insights into the interactions between VS and VW fault sections, showing that a weak, VS region weakens an adjacent VW region because interseismic creep in the VS region can penetrate into the VW section effectively causing "asperity erosion." Overall, this study significantly contributes to the understanding of basic slip behavior in relation to the  $L/h^*$ . It serves as a foundation for further experimental investigation into higher  $L/h^*$  (e.g., larger than 100), which more closely matches the behavior of large earthquakes on mature faults as explored in numerical studies (Michel et al., 2017; Sathiakumar & Barbot, 2021).

## **Appendix A: Friction Properties of Teflon Surface Treatment**

We refer to the first  $\sim$ 4 mm of slip on the interface as a run-in phase since a constant  $\tau_{\rm mech}$  has not been reached, as shown in Figure A1. When exploring if friction properties changed with longer-term displacement, we found that a run-in phase at a higher level of normal stress (i.e.,  $\sigma_n = 16$  MPa) was required to produce consistent results. To illustrate this, a set of six experimental runs are shown in Figure A1, performed in the following order (2, 16, 4, 8, 2, and 16 MPa). The first two experiments are denoted "1st Exp" to distinguish them from others ("2nd Exp") performed at the same  $\sigma_n$  levels. By comparing the results at  $\sigma_n = 2$  MPa between the 1st and 2nd experiments, it is evident that the friction coefficient and (a - b) significantly vary, whereas similar values were observed at 16 MPa (Figures A1c and A1d). The value of (a - b) gradually reduced with an increase in normal stress. This means that the slip behavior becomes more velocity neutral with an increase in normal stress. Nonetheless, it shows VS slip behavior even at 16 MPa.

SONG AND MCLASKEY 13 of 16

21699356, 2024, 4, Downloaded from https://agupubs.onlinelibary.wiley.com/doi/10.1029/2023JB028509 by Cornell University, Wiley Online Library on [15/07/2024]. See the Terms and Conditions (https://agupubs.onlinelibary.wiley.com/doi/10.1029/2023JB028509 by Cornell University, Wiley Online Library on [15/07/2024]. See the Terms and Conditions (https://agupubs.onlinelibary.wiley.com/doi/10.1029/2023JB028509 by Cornell University, Wiley Online Library on [15/07/2024]. See the Terms and Conditions (https://agupubs.onlinelibary.wiley.com/doi/10.1029/2023JB028509 by Cornell University, Wiley Online Library on [15/07/2024]. See the Terms and Conditions (https://agupubs.onlinelibary.wiley.com/doi/10.1029/2023JB028509 by Cornell University, Wiley Online Library on [15/07/2024]. See the Terms and Conditions (https://agupubs.onlinelibary.wiley.com/doi/10.1029/2023JB028509 by Cornell University, Wiley Online Library on [15/07/2024]. See the Terms and Conditions (https://agupubs.onlinelibary.wiley.com/doi/10.1029/2023JB028509 by Cornell University, Wiley Online Library on [15/07/2024]. See the Terms and Conditions (https://agupubs.onlinelibary.wiley.com/doi/10.1029/2023JB028509 by Cornell University, Wiley Online Library on [15/07/2024]. See the Terms and Conditions (https://agupubs.onlinelibary.wiley.com/doi/10.1029/2023JB028509 by Cornell University.wiley.com/doi/10.1029/2023JB028509 by Cornell University.

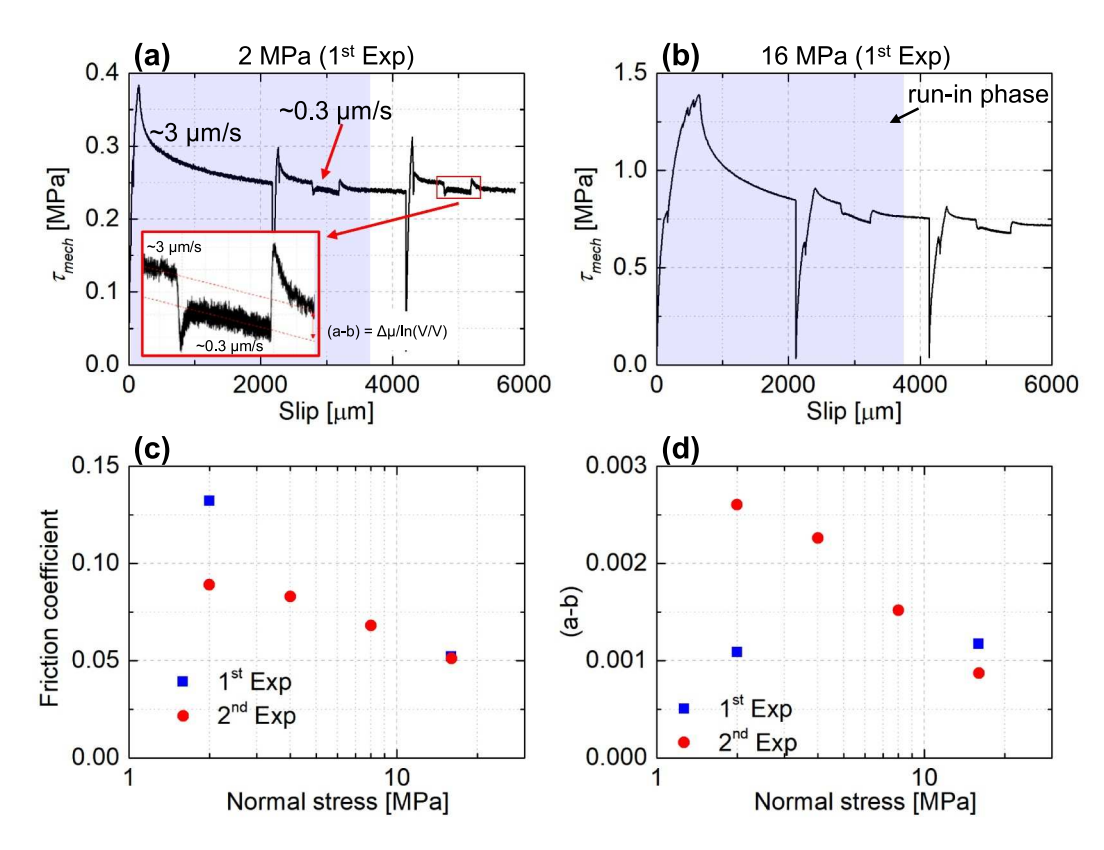


Figure A1. Velocity step tests for experiments with 760T configuration (Figure 1b) where the Teflon surface treatment was applied to the entire 760 mm fault. (a, b) Friction curves show  $\sim$ 4 mm of slip is required before properties stabilize. The imposed loading velocity was alternated between  $\sim$ 3 and  $\sim$ 0.3  $\mu$ m/s to obtain the rate-and-state friction (RSF) parameter. The shear stress was applied up to 2 mm of slip, released, and then re-applied. (c) The friction coefficient found from sample-average shear and normal stresses and (d) RSF parameter (a - b) found from velocity step tests are shown at different normal stress levels.

## **Data Availability Statement**

Data is freely available at Song and McLaskey (2024) and through Cornell eCommons at: https://doi.org/10.7298/dkwh-c932.

## Acknowledgments

The authors gratefully acknowledge that this work was funded by National Science Foundation Grant EAR-2240375. We also thank Sara Beth L. Cebry for assistance with the digital image correlation analysis. Data reported in this paper were acquired from laboratory experiments conducted at Cornell University.

#### References

Aki, K. (1966). Estimation of earthquake moment released energy and stress-strain drop from G-wave spectrum. Bulletin of the Earthquake Research Institute.

Ampuero, J.-P., & Rubin, A. M. (2008). Earthquake nucleation on rate and state faults – Aging and slip laws. *Journal of Geophysical Research*, 113(B1), B01302. https://doi.org/10.1029/2007JB005082

Barbot, S. (2019). Slow-slip, slow earthquakes, period-two cycles, full and partial ruptures, and deterministic chaos in a single asperity fault. *Tectonophysics*, 768(July), 228171. https://doi.org/10.1016/j.tecto.2019.228171

Bedford, J. D., Faulkner, D. R., & Lapusta, N. (2022). Fault rock heterogeneity can produce fault weakness and reduce fault stability. *Nature Communications*, 13(1), 326. https://doi.org/10.1038/s41467-022-27998-2

Buijze, L., Guo, Y., Niemeijer, A. R., Ma, S., & Spiers, C. J. (2020). Nucleation of stick-slip instability within a large-scale experimental fault: Effects of stress heterogeneities due to loading and gouge layer compaction. *Journal of Geophysical Research: Solid Earth*, 125(8), e2019JB018429. https://doi.org/10.1029/2019JB018429

Buijze, L., Guo, Y., Niemeijer, A. R., Ma, S., & Spiers, C. J. (2021). Effects of heterogeneous gouge segments on the slip behavior of experimental faults at dm scale. Earth and Planetary Science Letters, 554, 116652. https://doi.org/10.1016/j.epsl.2020.116652

Cattania, C. (2019). Complex earthquake sequences on simple faults. *Geophysical Research Letters*, 46(17–18), 10384–10393. https://doi.org/10.1030/2010/CI.082428

Cebry, S. B. L., Ke, C. Y., Shreedharan, S., Marone, C., Kammer, D. S., & McLaskey, G. C. (2022). Creep fronts and complexity in laboratory earthquake sequences illuminate delayed earthquake triggering. *Nature Communications*, 13(1), 1–9. https://doi.org/10.1038/s41467-022-34397-0

Cebry, S. B. L., & McLaskey, G. C. (2021). Seismic swarms produced by rapid fluid injection into a low permeability laboratory fault. Earth and Planetary Science Letters, 557, 116726. https://doi.org/10.1016/j.epsl.2020.116726

Cebry, S. B. L., Sorhaindo, K., & McLaskey, G. C. (2023). Laboratory earthquake rupture interactions with a high normal stress bump. *Journal of Geophysical Research: Solid Earth*, 128(11), 1–24. https://doi.org/10.1029/2023JB027297

SONG AND MCLASKEY 14 of 16

21699356, 2024, 4, Downloaded

- Chen, T., & Lapusta, N. (2009). Scaling of small repeating earthquakes explained by interaction of seismic and aseismic slip in a rate and state fault model. *Journal of Geophysical Research*, 114(1), 1–12. https://doi.org/10.1029/2008JB005749
- Dieterich, J. H. (1979). Modeling of rock friction: 1. Experimental results and constitutive equations. *Journal of Geophysical Research*, 84(B5), 2161–2168. https://doi.org/10.1029/JB084iB05p02161
- Dieterich, J. H. (1992). Earthquake nucleation on faults with rate-and state-dependent strength. *Tectonophysics*, 211(1–4), 115–134. https://doi.org/10.1016/0040-1951(92)90055-B
- Dieterich, J. H., & Kilgore, B. D. (1994). Direct observation of frictional contacts: New insights for state-dependent properties. *Pure and Applied Geophysics*, 143(1–3), 283–302. https://doi.org/10.1007/BF00874332
- Giorgetti, C., Carpenter, B. M., & Collettini, C. (2015). Frictional behavior of talc-calcite mixtures. *Journal of Geophysical Research: Solid Earth*, 120(9), 6614–6633. https://doi.org/10.1002/2015JB011970
- Guérin-Marthe, S., Nielsen, S., Bird, R., Giani, S., & Di Toro, G. (2019). Earthquake nucleation size: Evidence of loading rate dependence in laboratory faults. *Journal of Geophysical Research: Solid Earth*, 124(1), 689–708. https://doi.org/10.1029/2018JB016803
- Ito, Y., Obara, K., Shiomi, K., Sekine, S., & Hirose, H. (2007). Slow earthquakes coincident with episodic tremors and slow slip events. *Science*, 315(5811), 503–506. https://doi.org/10.1126/science.1134454
- Kaneko, Y., & Lapusta, N. (2008). Variability of earthquake nucleation in continuum models of rate-and-state faults and implications for aftershock rates. *Journal of Geophysical Research*, 113(12), 1–25. https://doi.org/10.1029/2007JB005154
- Kaneko, Y., Nielsen, S. B., & Carpenter, B. M. (2016). The onset of laboratory earthquakes explained by nucleating rupture on a rate-and-state fault. *Journal of Geophysical Research: Solid Earth*, 121(8), 6071–6091. https://doi.org/10.1002/2016JB013143
- Lapusta, N., & Liu, Y. (2009). Three-dimensional boundary integral modeling of spontaneous earthquake sequences and aseismic slip. *Journal of Geophysical Research*, 114(9), 1–25. https://doi.org/10.1029/2008JB005934
- Lapusta, N., & Rice, J. R. (2003). Nucleation and early seismic propagation of small and large events in a crustal earthquake model. *Journal of Geophysical Research*, 108(B4), 1–18. https://doi.org/10.1029/2001jb000793
- Leeman, J. R., Saffer, D. M., Scuderi, M. M., & Marone, C. (2016). Laboratory observations of slow earthquakes and the spectrum of tectonic fault slip modes. *Nature Communications*, 7(1), 11104. https://doi.org/10.1038/ncomms11104
- Sup induces, value communications, 7(1), 11104. https://doi.org/10.1036/incommis/1104
  Lu, X. (2009). Combined experimental and numerical study of spontaneous dynamic rupture on frictional interfaces. California Institute of Technology.
- Lui, S. K. Y., & Lapusta, N. (2016). Repeating microearthquake sequences interact predominantly through postseismic slip. *Nature Communications*, 7, 1–7. https://doi.org/10.1038/ncomms13020
- Lui, S. K. Y., & Lapusta, N. (2018). Modeling high stress drops, scaling, interaction, and irregularity of repeating earthquake sequences near Parkfield. Journal of Geophysical Research: Solid Earth, 123(12), 10854–10879. https://doi.org/10.1029/2018JB016472
- Luo, Y., & Ampuero, J.-P. (2018). Stability of faults with heterogeneous friction properties and effective normal stress. *Tectonophysics*,
- 733(October 2017), 257–272. https://doi.org/10.1016/j.tecto.2017.11.006

  Marone, C. (1998). Laboratory-derived friction laws and their application to seismic faulting. Annual Review of Earth and Planetary Sciences,
- 26(1), 643–696. https://doi.org/10.1146/annurev.earth.26.1.643

  McLaskey, G. C. (2019). Earthquake initiation from laboratory observations and implications for foreshocks. *Journal of Geophysical Research:*See A. (2012). 12882. 12004. https://doi.org/10.1020/2014/PD418262
- Solid Earth, 124(12), 12882–12904. https://doi.org/10.1029/2019JB018363

  Mclaskey, G. C., & Yamashita, F. (2017). Slow and fast ruptures on a laboratory fault controlled by loading characteristics. Journal of
- Geophysical Research: Solid Earth, 122(5), 3719–3738. https://doi.org/10.1002/2016JB013681

  Mei, C., Barbot, S., Jia, Y., & Wu, W. (2022). Experimental evidence for multiple controls on fault stability and rupture dynamics. Earth and
- Planetary Science Letters, 577, 117252. https://doi.org/10.1016/j.epsl.2021.117252

  Mei, C., Barbot, S., & Wu, W. (2021). Period-Multiplying cycles at the transition between stick-slip and stable sliding and implications for the Parkfield period-doubling tremors. Geophysical Research Letters, 48(7), 1–13. https://doi.org/10.1029/2020GL091807
- Michel, S., Avouac, J., Lapusta, N., & Jiang, J. (2017). Pulse-like partial ruptures and high-frequency radiation at creeping-locked transition during megathrust earthquakes. *Geophysical Research Letters*, 44(16), 8345–8351. https://doi.org/10.1002/2017GL074725
- Moore, D. E., & Rymer, M. J. (2007). Talc-bearing serpentinite and the creeping section of the San Andreas fault. *Nature*, 448(7155), 795–797. https://doi.org/10.1038/nature06064
- Nakata, R., Ando, R., Hori, T., & Ide, S. (2011). Generation mechanism of slow earthquakes: Numerical analysis based on a dynamic model with
- brittle-ductile mixed fault heterogeneity. *Journal of Geophysical Research*, 116(B8), B08308. https://doi.org/10.1029/2010JB008188

  Obara, K., Hirose, H., Yamamizu, F., & Kasahara, K. (2004). Episodic slow slip events accompanied by non-volcanic tremors in southwest Japan subduction zone. *Geophysical Research Letters*, 31(23), 1–4. https://doi.org/10.1029/2004GL020848
- Obara, K., & Kato, A. (2016). Connecting slow earthquakes to huge earthquakes. *Science*, 353(6296), 253–257. https://doi.org/10.1126/science.
- Rice, J. R., & Ruina, A. L. (1983). Stability of steady frictional slipping. *Journal of Applied Mechanics*, 50(2), 343–349. https://doi.org/10.1115/1.
- Rubin, A. M., & Ampuero, J.-P. (2005). Earthquake nucleation on (aging) rate and state faults. *Journal of Geophysical Research*, 110(B11), 1–24. https://doi.org/10.1029/2005JB003686
- Ruina, A. (1983). Slip instability and state variable friction laws. *Journal of Geophysical Research*, 88(B12), 10359–10370. https://doi.org/10. 1029/JB088iB12p10359
- Sathiakumar, S., & Barbot, S. (2021). The stop-start control of seismicity by fault bends along the Main Himalayan Thrust. Communications Earth & Environment, 2(1), 87. https://doi.org/10.1038/s43247-021-00153-3
- Scholz, C. H. (1998). Earthquakes and friction laws. Nature, 391(6662), 37-42. https://doi.org/10.1038/34097
- Scuderi, M. M., Marone, C., Tinti, E., Di Stefano, G., & Collettini, C. (2016). Precursory changes in seismic velocity for the spectrum of earthquake failure modes. *Nature Geoscience*, 9(9), 695–700. https://doi.org/10.1038/ngeo2775
- Song, J. Y., & McLaskey, G. C. (2024). Laboratory earthquake ruptures contained by velocity strengthening fault patches [Dataset]. *Cornell eCommons*. Retrieved from https://ecommons.cornell.edu/handle/1813/113835
- Titus, S. J., DeMets, C., & Tikoff, B. (2006). Thirty-five-year creep rates for the creeping segment of the San Andreas fault and the effects of the 2004 Parkfield earthquake: Constraints from alignment arrays, continuous global positioning system, and creepmeters. *Bulletin of the Seismological Society of America*, 96(4B), S250–S268. https://doi.org/10.1785/0120050811
- Veedu, D. M., & Barbot, S. (2016). The Parkfield tremors reveal slow and fast ruptures on the same asperity. Nature, 532(7599), 361–365. https://doi.org/10.1038/nature17190
- Veedu, D. M., Giorgetti, C., Scuderi, M., Barbot, S., Marone, C., & Collettini, C. (2020). Bifurcations at the stability transition of earthquake faulting. Geophysical Research Letters, 47(19), 1–10. https://doi.org/10.1029/2020GL087985

SONG AND MCLASKEY 15 of 16



# Journal of Geophysical Research: Solid Earth

10.1029/2023JB028509

- Wallace, L. M., Webb, S. C., Ito, Y., Mochizuki, K., Hino, R., Henrys, S., et al. (2016). Slow slip near the trench at the Hikurangi subduction zone, New Zealand. Science, 352(6286), 701–704. https://doi.org/10.1126/science.aaf2349
- Wu, B. S., & McLaskey, G. C. (2019). Contained laboratory earthquakes ranging from slow to fast. *Journal of Geophysical Research: Solid Earth*, 124(10), 10270–10291. https://doi.org/10.1029/2019JB017865
- Xu, S., Fukuyama, E., Yamashita, F., Mizoguchi, K., Takizawa, S., & Kawakata, H. (2018). Strain rate effect on fault slip and rupture evolution: Insight from meter-scale rock friction experiments. *Tectonophysics*, 733, 209–231. https://doi.org/10.1016/j.tecto.2017.11.039
- Yamashita, F., Fukuyama, E., & Xu, S. (2022). Foreshock activity promoted by locally elevated loading rate on a 4-m-Long laboratory fault. Journal of Geophysical Research: Solid Earth, 127(3), e2021JB023336. https://doi.org/10.1029/2021JB023336

SONG AND MCLASKEY 16 of 16